Materials Science and Engineering B 276 (2022) 115558

Contents lists available at ScienceDirect

Materials Science & Engineering B

journal homepage: www.elsevier.com/locate/mseb

Silver-enriched ZnO:Ag thin films deposited by magnetron co-sputtering: Post annealing effects on structural and physical properties

Rehab Ramadan [a,b], S. Dadgostar [c], M. Manso –Silván [a,e], R. Pérez-Casero [a,e], M. Hernandez-Velez [a], J. Jimenez [c], O. Sanchez [d,*]

[a] Applied Physics Department, Universidad Autónoma de Madrid, 28049 Cantoblanco, Madrid, Spain
[b] Faculty of Science, Minia University, 61519 Minia, Egypt
[c] GdS Optronlab, Ed. LUCIA, EII, Universidad de Valladolid, Paseo de Belén 19, 47011 Valladolid, Spain
[d] Instituto de Ciencia de Materiales de Madrid (CSIC) .C/Sor Juana Inés de la Cruz, 3. 28049 Madrid, Spain
[e] Centro de Microanálisis de Materiales and Instituto de Ciencia de Materiales Nicolás Cabrera, Universidad Autónoma de Madrid, 28049 Cantoblanco, Madrid, Spain

ARTICLE INFO

Keywords:
ZnO:Ag compounds
DC Magnetron Sputtering
RBS and XRD analysis
Optical and Electrical characterization
Ag plasmonic effect

ABSTRACT

The ZnO semiconductor is probably among the most mentioned compounds in the scientific literature during the last decade, which is mainly due to its wide spectrum of applications. Compounds based on ZnO (in doped or composite form) are of great relevance for the development of high-tech devices. In this work, we present the growth and characterization of samples deposited by DC Magnetron co-sputtering from two pure Zn and Ag targets in an O_2 / Ar atmosphere. The samples were characterized as deposited and after an annealing treatment in a reducing atmosphere. We have used XRD, RBS, ellipsometry, UV visible photoluminescence, and electrical measurements for sample characterization. The results revealed the amorphization of ZnO when the Ag content increases and, after annealing, a mixture of crystalline phases was detected for the samples with higher Ag content. It is also demonstrated the strong effect of the presence of Ag atoms in the stimulated optical and electrical responses from ZnO:Ag compounds obtained in this work.

1. Introduction

Zinc Oxide (ZnO), is a II-VI semiconductor that has received great attention throughout the last decades because of its multi-functional properties making it suitable for many applications. Some of the remarkable properties allowing the high ZnO functionality are: a high photo-activity, n-type conductivity, wide band gap energy, strong oxidizing power, non-toxicity, high transparency in the visible near-UV range, piezoelectricity, chemical stability and biocompatibility, among others[1–9].

Up to date, the most relevant ZnO applications are in the field of micro- and opto-electronic devices, e.g. thin-film transistors (TFTs), ultraviolet resistive coatings, gas sensors and UV photo-detectors. Other remarkable applications can be found in the field of photocatalysis, in magnetic semiconductors, but also as an antimicrobial agent, inhibiting both Gram-positive and Gram-negative bacteria [10–18].

Great attention is being paid to the improvement of the optical and electrical behaviour of ZnO films with the incorporation of a noble metal to its structure (Pt, Au, Ag and Pd) [19–23]. In this sense, there are antecedents about the incorporation of noble metals in semiconductors aiming to increase the photocatalytic efficiency [24]. The incorporation of noble metals to ZnO boosts the photocatalytic activity in the visible spectral range by means of the surface plasmon resonance (SPR), which enhances the visible light absorption [22]. Furthermore, the rate of the electron-hole pair recombination is slowed down by the formation of a Schottky barrier [23].

Among the noble metal candidates to be incorporated into ZnO matrices, silver stands out for its excellent electrical, optical and chemical properties that allow not only to improve ZnO photocatalytic activity, but also changing the conductive type and luminescence properties[22]. Furthermore, the Ag addition in ZnO matrix leads to an improvement of its antibacterial activity [25].

Growth of ZnO thin films and nanostructures incorporating silver has been made by different methods e.g. ion implantation, pulsed laser deposition, microwave techniques, chemical reactions in aqueous solutions, etc. [26–29]. The choice of the most suitable ZnO: Ag growth method and the comprehension of the Ag incorporation in the ZnO lattice (either as a dopant, or forming aggregates, or mixed oxide form), is still under debate.

In this work, we used a DC magnetron co-sputtering system for ZnO

* Corresponding author.

https://doi.org/10.1016/j.mseb.2021.115558
Received 16 December 2020; Received in revised form 31 August 2021; Accepted 25 November 2021
Available online 4 December 2021
0921-5107/© 2021 The Author(s). Published by Elsevier B.V. This is an open access article under the CC BY-NC-ND license (http://creativecommons.org/licenses/by-nc-nd/4.0/).

and ZnO:Ag thin film deposition. This technique allows the control of the elemental composition of the resulting films by properly adjusting the process parameters. Moreover, the sputtering deposition is widely used for thin film growth due to its ability to coat large surface areas, making it easy to scale-up industrially. Most of the works related to ZnO:Ag growth by magnetron co-sputtering use ZnO and Ag targets [30]. In this work, pure metallic Zn and Ag targets are used within an O_2 reactive atmosphere allowing to enlarge the range of Ag concentration values in the ZnO matrix.

In order to further investigate the effect of Ag addition on the properties of ZnO films, we present hereinafter structural, electrical and optical characterization of ZnO films with different Ag contents before and after thermal annealing in H_2 atmosphere at 300℃.

2. Experimental

ZnO:Ag films were deposited on both <100>oriented silicon samples (resistivity > 6000 Ω·cm) and quartz glass slides, by reactive magnetron co-sputtering in a home-made system. The reaction chamber consists of a cylindrical vacuum chamber where two circular planar magnetrons (3 in. diameter) were located forming an angle of 60° between them, so that the samples were exposed to both cathodes during the growth processes. Highly pure commercial Zinc (99.99%) and Silver (99.99%) targets (Neyco supplier) were employed. All experiments were performed in an Ar (99.999%) and O_2 (99.992%) atmosphere maintaining the relative O_2 concentration at 24%. The chamber was pumped out to a base pressure of 3×10^{-6} hPa being the working pressure at 7.4×10^{-3}hPa. Before deposition, the Zn and Ag targets were pre-sputtered for 10 min to remove any surface impurity. The substrates were cleaned in successive ultrasonic baths to degrease and to eliminate the rest of foreign materials on their surfaces. Finally, they were dried under nitrogen flow. Two independent cathodes (Ag and Zn) fed with different power were used to control the Ag/Zn relative content in the samples. The samples were grown after the total poisoning of the targets working under the reactive sputtering regime. Even though no intentional heating was applied to the substrate, a temperature between 90 and 100 °C was reached during deposition because of impact of incident atoms. A set of samples were grown, in which the power applied to de Zn cathode (P_{Zn}) was kept constant at 100 W and the power applied to de Ag cathode (P_{Ag}) was varied in the 0–100 W range. The deposition time was adjusted in order to obtain film thicknesses below 200 nm. The deposition conditions, film thicknesses and samples densities are given in Table 1. The ZnO:Ag samples were annealed in a reducing atmosphere at 300 °C using an H_2:Ar gas mixture with an equivalent flow rate of 3:2 at atmospheric pressure for 30 min.

The thickness and composition of the ZnO:Ag films were measured by Rutherford Backscattering Spectrometry (RBS) using the 5 MV Cockroft-Walton tandetron facility at the Centro de Microanálisis de Materiales (CMAM) in Madrid (Spain). A 2.0 MeV He^+ beam impinged at normal incidence with respect to the sample surface and the back-scattered ions were detected with a silicon detector at a scattering angle of 170°. The RBS spectra were simulated with the SIMNRA code [31] to provide a quantitative analysis. Zinc and Silver contents of the film were determined with a 1–2 % accuracy, while the oxygen content was only determined with 4% precision, owing to the low RBS yield for light elements. The film thicknesses were also measured using a mechanical stylus profilometer (Veeco Dektak 150).

Table 1
Sample labels, deposition conditions, thicknesses and density. The atomic density is determined from the thicknesses measured by profilometry and calculated by RBS analysis.

Sample	P_{Zn} (W)	P_{Ag} (W)	Dep. rate (nm/min ± 10%)	Thickness (nm ± 10%)	Thickness (10^{15} at/cm^2)	Density (10^{22} at/cm^3)
Z0	100	0	3.33	100	660	6.6
ZA1		20	12.6	190	1370	7.2
ZA2		30	17.5	175	1130	6.4
ZA3		50	24.0	120	785	6.5
ZA4		100	41	125	730	5.8

The crystalline structure of ZnO films with different Ag contents was identified using grazing incidence X ray diffraction at 0.5° incidence angle (Siemens D 5000, with Cu anode, Kα radiation = 1.54178 Å). Morphology of the ZnO:Ag thin films was observed by scanning electron microscopy (Hitachi S-3000Nps) and the surface resolved energy dispersive analysis was performed with a Quantax XFlash 6I30 analyzer (Bruker). The surface features of SEM images were analyzed using ImageJ software.

The optical properties of the thin films were analyzed by ellipsometry and photoluminescence measurements (PL). The ellipsometry measurements were performed with a J.A. Woollam Co. VASE ellipsometer in the 250–1450 nm range at 70° angle with respect to the surface normal. The results were fitted according to modified ZnO models taking into account the Ag component and the reduction annealing process (Complete EASE software, J.A. Woollam Co.). The ZnO control layer was fitted using a model considering the optical properties of an aluminum doped ZnO thin film [32] on top of a Si substrate with native oxide layer. For ZnO:Ag layers, two materials effective medium approximation (EMA) model consisting of ZnO and Ag was considered. The composition and thickness of the layer are fitting parameters. Photoluminescence (PL) measurements were carried with a Labram UV-HR 800 Raman spectrometer from Horiba-Jobin Yvon using 150 g/mm grating at room temperature. The excitation and the light collection were performed by means of a confocal metallographic microscope with an ultraviolet (UV) high magnification objective (40X) and 0.47 numerical aperture (NA) from OFR- Optics for research. The 325 nm line of a He-Cd laser was used as the excitation source. The laser beam diameter in the focal plane was below 1 μm according to the Abbe formula ($\phi = 1.22\ \lambda/NA$). The spectra were recorded at different zones on each sample in order to check the homogeneity. Due to the spectrometer configuration, the spectra were acquired in two different spectral intervals using two sets of filters: UV filters between 320 nm and 450 nm, and visible filters in the range from 450 nm to 850 nm. On the other hand, the zones taken in the different ranges are not exactly coincident. This procedure prevents a one to one comparison of the spectra recorded in the two spectral ranges

The electrical performance of the ZnO and ZnO:Ag samples was analyzed by electrochemical impedance spectroscopy (EIS) using a Bio-Logic SP- 150 potentiostat (Seyssinet-Pariset, France). Au point contacts were deposited on the thin film surface by direct current (DC) sputtering. The electrical measurements were produced inside a Faraday cage to shield the system from external signals. The alternating current (AC) impedance measurements were carried out between two points on the surface of the samples in the 100 Hz −700 kHz frequency range, with 0.5 V excitation potential. The data fitting to equivalent electrical circuits was performed using the EC-Lab software from Bio- Logic Science Instruments. The current -voltage (I-V) curves in the range from −1 to + 1 V were plotted for the mentioned thermally treated ZnO and ZnO:Ag samples with a scan rate of 20 mV/s.

3. Results and discussion

The RBS spectra of as deposited samples are shown in Fig. 1. The backscattering yield for each element is proportional to the convolution of its areal density and corresponding Rutherford cross-section. The dependence of the Zn and Ag yields as a function of the power applied to the Ag target shows that the higher the power applied to the Ag cathode, the higher the Ag content of the films. In addition, the Ag deposition rate is much higher than that of Zn (see Table 1).

Moreover, the respective shapes of Zn and Ag rear edge and Si

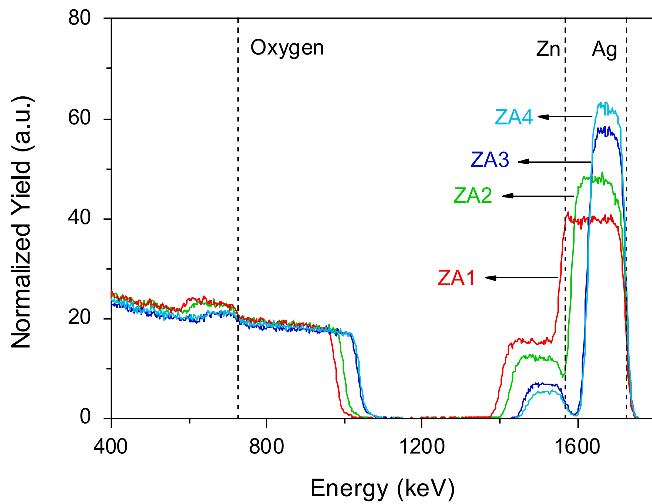

Fig. 1. Backscattering spectra of the samples. Dot lines indicate the surface energy locations of different elements.

leading edge of the backscattering contributions indicate that the interface between the ZnO film and Si substrate is sharp, suggesting that no interfacial reactions occurred during the growth process. On the other hand, the flatness of the signals corresponding to the different elements reflects the homogeneity of the samples.

The film composition as a function of the power applied to the silver target, as obtained by the simulation of the experimental spectra, is presented in Fig. 2.The results pinpoint the increase in the Ag concentration and the concomitant decrease in the Zn one as the power on Ag cathode increases. The inset shows that the Ag/Zn concentration ratio depends roughly linearly on the Ag/Zn power ratio, except for the highest Ag/Zn power ratios where Ag/Zn concentration ratio tends to saturate.

The XRD patterns recorded for as deposited and annealed samples are plotted in Fig. 3. In the as-grown ZnO film diffractogram, one can see only three peaks at 34.5, 56.7 and 62.8, 2θ degrees attributed to ZnO ⟨0 0 2⟩, ⟨1 1 0⟩ and ⟨1 0 3⟩ crystal planes, respectively. This result allows us to identify the typical polycrystalline ZnO with hexagonal (wurtzite) structure (JCPDS card N° 36–1451) [33] being the most intense Bragg reflection around the ⟨0 0 2⟩ direction. Nevertheless, the remarkable

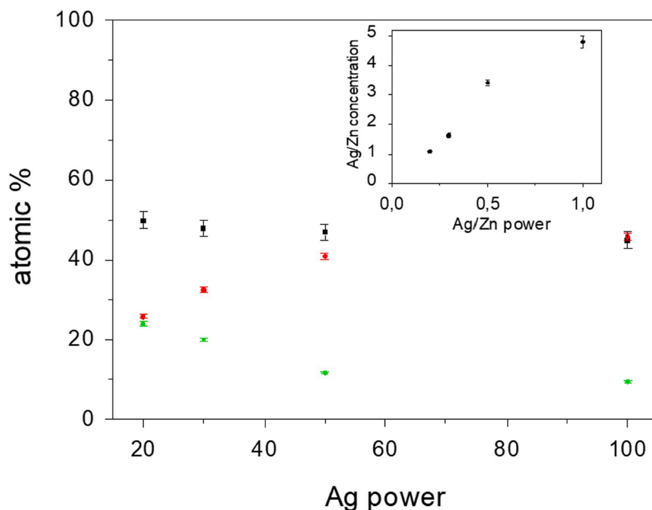

Fig. 2. Results achieved from the RBS analysis Composition of the films as a function of the power applied on Ag target (O: hollow square; Ag: hollow circle; Zn: solid circle). The inset shows the Ag/Zn concentration ratio as a function of the Ag/Zn power ratio.

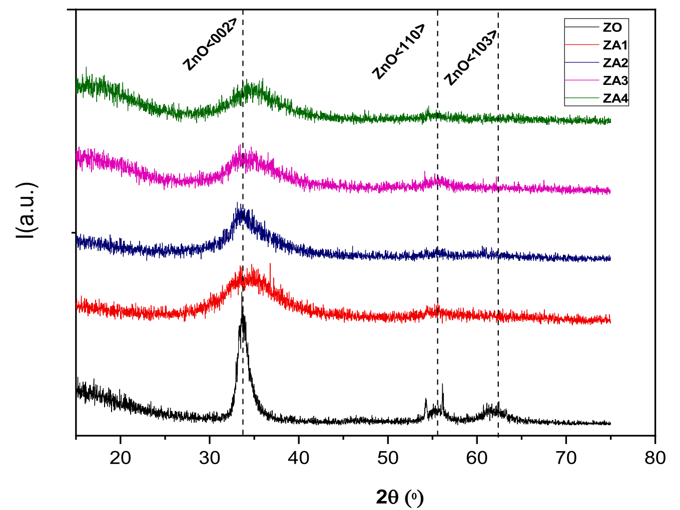

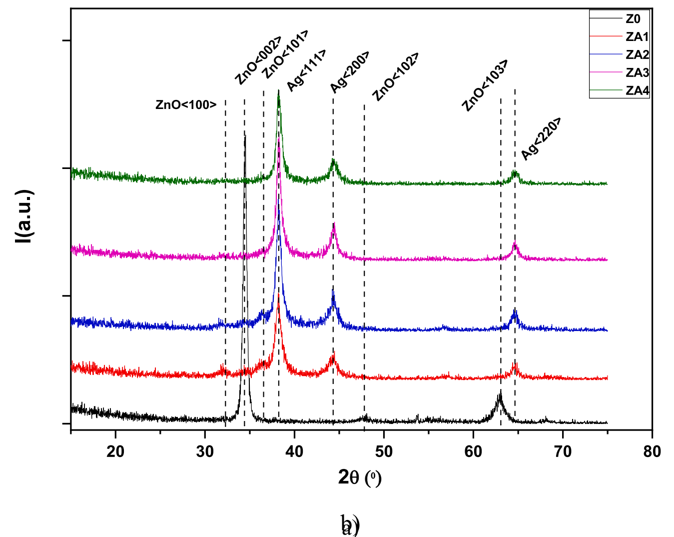

Fig. 3. X-ray diffractograms of samples: a) before annealing and b) after annealing in H_2 atmosphere at 300 °C.

width of these peaks denotes the low crystallinity of the film. This fact can be due to the relative position of the sample with respect to the Zn cathode in the magnetron co-sputtering deposition process. In the co-sputtering configuration, the substrate is located at an equidistant position from the two targets. So, the sample is simultaneously exposed to the Zn and Ag cathodes and the reactive species from the plasma generated near the Zn cathode reach the sample surface in an oblique angle [34].

As seen in Fig. 3a, in agreement with RBS results, the amount of Ag incorporated in the film increases as the power on the Ag target does, while the peaks corresponding to the ZnO ⟨1 1 0⟩ and ⟨1 0 3⟩ reflections disappear. XRD patterns of as deposited ZnO:Ag films show only a very broad band peaking around 34°and it indicates the amorphization of ZnO. No evident signals related to Ag, or its oxide phases were detected. Nevertheless, it is not discarded the existence of precursor seeds of different Ag compounds since some of them present Bragg reflections in the 2Θ range swept by this band [25]. This might be confirmed or not from the XRD patterns of the annealed samples. Additionally, the formation of amorphous phases is also intuited from the apparition of another broad band for the lowest 2Θ values, particularly in the spectrum of sample ZA4. These observations allow to suspect about the

formation of amorphous silver oxides which might be also suggested from the RBS spectra shown in Fig. 1, where it is clear that as the Ag incorporation increases, the Zn content decreases while the oxygen content only show a slight decrease.

XRD spectra of the annealed ZnO:Ag samples are displayed in Fig. 3b. In the case of the ZnO sample, the peak associated to the (0 0 2) planes experiences a large increase in intensity and noticeable narrowing, which clearly points out an improvement of the ZnO crystallinity. Similar behavior is observed for the ⟨1 0 3⟩ peak of ZnO. After annealing, all patterns of the samples containing silver show the most intense diffraction peaks corresponding to crystalline cubic Silver [25]. These diffraction peaks are located at 38.15°, 44.23° and 64.59°. In the case of samples ZA1 and ZA2 grown at 20 and 30 W, respectively three small peaks can be also observed in the 2θ range of 30°-40°, which could be associated to the ⟨1 0 0)>, ⟨0 0 2⟩ and ⟨1 0 1⟩ planes of wurtzite ZnO. The spectra of the samples with higher Ag contents, displayed only the diffraction peaks associated with the presence of crystalline Ag. After thermal treatment, according to the X-ray diffraction results, the samples with lower Ag/Zn ratio (below 1.6) present a crystalline structure looking as a composite formed by mixed hexagonal wurtzite ZnO and cubic Ag phases. However, in the case of samples with the highest Ag contents (i.e., ZA3 and ZA4), only the cubic crystalline structure of silver seems to be present, while the ZnO lattice appears to be amorphous or heavily distorted. These results can be understood assuming a possible silver segregation produced by the annealing, as was already reported in the literature [35]. Besides, the ZnO structure is distorted due to a high increase of O vacancies because the annealed/reduction conditions, which contribute to a certain disorder of the ZnO lattice. The silver crystallite size, D, was estimated according to the Scherer formula using the most intense Ag reflex ⟨1 1 1⟩ [36]:

$$D = kl/bcos\Theta \tag{1}$$

where k is the constant (k = 0.9), is the X-ray wavelength, b is the FWHM in radians and Θis the Bragg diffraction angle. The mean Ag crystallite size slightly varies for increasing Ag content tending to stabilize around 11 ± 0.5 nm for the ZnO:Ag films with the highest Ag content.

The morphologies of ZnO:Ag thin films after annealing were observed by SEM, as displayed in Fig. 4. Some “large” crystals were observed on the film surface accompanied by a dense array of smaller crystals, as shown in Fig. 4a. Increasing the Ag content in the films results in larger particle size on the sample surface (see 4a–d).

The optical properties of the ZnO:Ag films were analyzed by ellipsometry and photoluminescence (PL) in the UV and Visible ranges. Pure ZnO thin films were characterized as control samples in ellipsometry measurements. In Fig. 5, the resulting ellipsometric spectra are shown as a function of incident wavelength for typical samples Z0 and ZA3. The plotted curves include acquired and simulated data [37] used to obtain complementary information such as thickness and composition. The reasonably good agreement between experimental and simulated ellipsometry spectra in Fig. 5a was achieved using a thickness for the control ZnO film of 110 nm as simulation parameter, which is in good agreement with that measured by means of profilometry (see Table 1). The as-sputtered ZnO:Ag films presented a characteristic interferometric behavior.

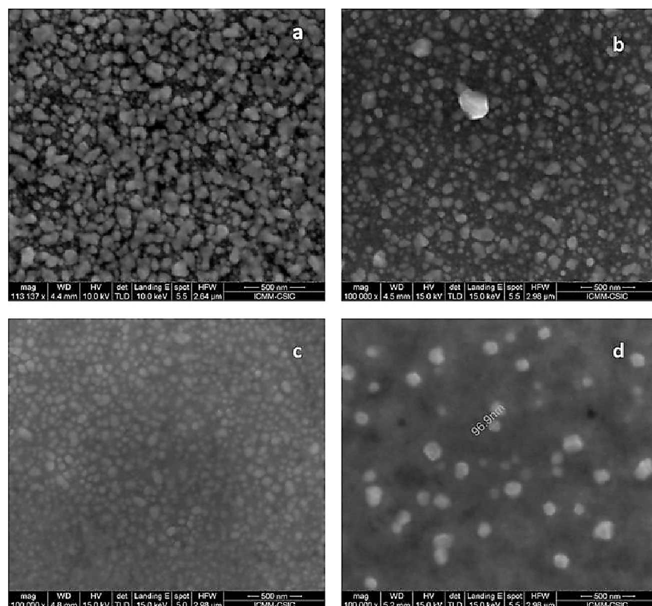

Fig. 4. SEM images of ZnO:Ag films after annealing, a) ZA1, b) ZA2, c) ZA3, d) ZA4.

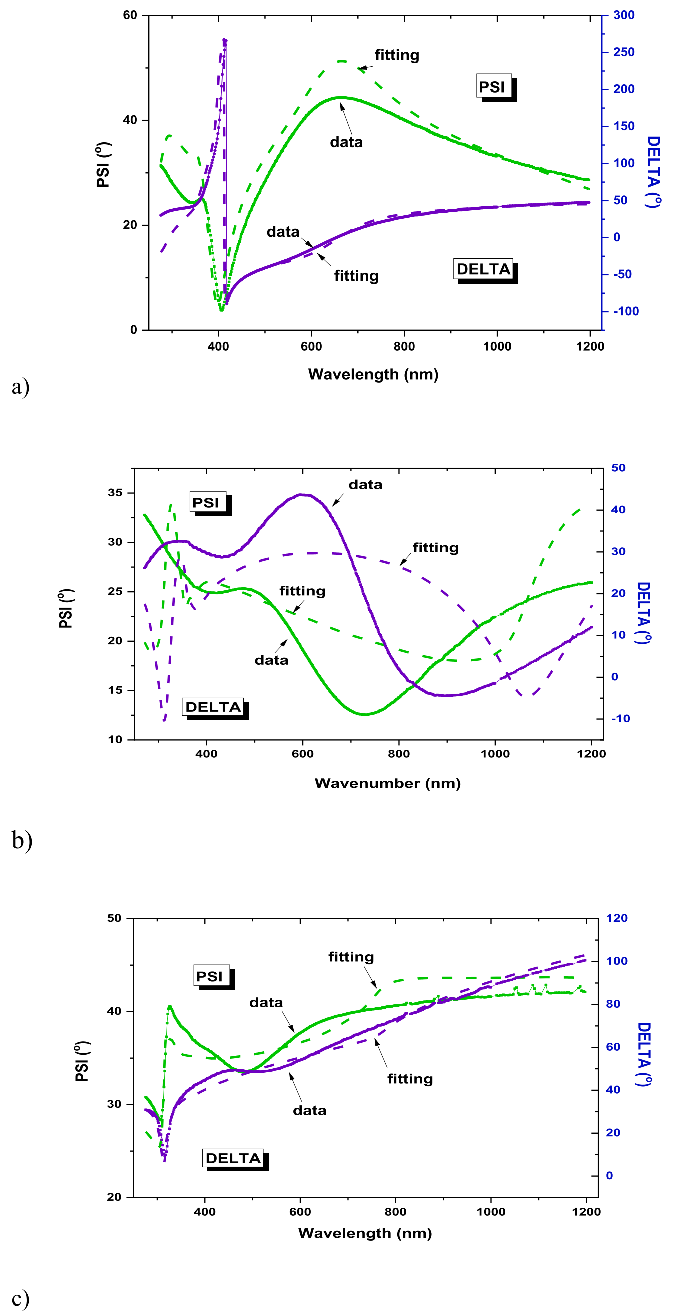

Fig. 5. Psi and Delta ellipsometric functions for different ZnO:Ag films. a) Pure ZnO control sample. b) ZA3 film and, c) ZA3 film after reduction/annealing process.

The difficulties to obtain adequate fitting functions to the experimental data were inherent to the lack of an appropriate ZnO:Ag alloy model. As a illustrative example, the behavior of the ZA3 film deposited with 50 W in the Ag cathode is shown in Fig. 5b. The simulation lines just illustrate the difficulties to fit the results with an Ag-ZnO composite model consisting of an effective medium incorporating the independent properties of Ag and ZnO with variable amounts of one phase with respect to the other.

On the other hand, the samples showed a characteristic behavior after the reduction/annealing process. Taking again the ZA3 sample, a good qualitative agreement can be found between experimental and simulated results, as presented in Fig. 5c. The qualitative agreement between the experimental and modeling ellipsometric parameters confirms that the reduction/annealing process is effective in inducing a phase separation. The 70 nm thick films behave as Ag/ZnO nanocomposites consisting of 67 vol% Ag (75 at.%) rather than as homogeneous ZnO:Ag compounds. The most relevant feature of these films is the observation of a clear Ag plasmonic effect, as derived from the features of the ellipsometric functions at around 300 nm wavelength. This behavior was identified in all the reduced ZnO:Ag samples.

In order to confirm the potential microstructural change induced during the reduction/annealing process, we performed a simultaneous SEM/imaging EDX analysis. In fact, the presence of segregated clusters on the surfaces of annealed ZnO:Ag samples was confirmed, as shown in the SEM image of Fig. 6a. The observed surface clusters present a heterogeneous size distribution ranging from a few tens and up to 400 nm. However, the biggest clusters outstand because they present faceting, suggesting a crystalline state, as confirmed by XRD. In order to identify the nature of the clusters, the surfaces were analyzed by imaging EDX. The results are shown in Fig. 6b, in superposition with the SEM image.

The color labelling clearly illustrates that the segregated clusters consist of Ag, although this element remains also distributed all over the film. Meanwhile, Zn appears exclusively as a homogeneously distributed element. From the point of view of the processing, these results confirm that the reduction step is Ag selective, promoting the segregation in clusters, meanwhile, Zn remains forming the surrounding host ZnO matrix. This result is in agreement with the amorphous ZnO phase suggested in the interpretation of the XRD data obtained for the as-deposited samples and particularly clear in the XRD data of ZA1 sample.

The PL spectra of as-deposited ZnO and ZnO:Ag samples in the UV range are shown in Fig. 7a. The reference sample of ZnO presents a band centered around 3.26 eV and associated with the near band edge (NBE) emission in wurtzite ZnO. This transition at room temperature is dominated by the phonon replicas of the free exciton, peaking at the FX-1LO replica [38]. Its width, ≈0.2 eV, larger than that of ZnO crystals, ≈ 0.1 eV, suggests the contribution of defects and/or disorder in agreement with XRD measurements. Regarding the Ag doped samples, one observes that the presence of Ag reduces the PL intensity with respect to the ZnO sample, and modifies the spectrum shape. One can fit the spectra with three Gaussian bands, labeled A, B, and C. The positions of these bands depend on the Ag content. Blue-violet, band A, peaks around 3 eV, band B peaks between 3.2 and 3.3 eV and band C peaks between 3.35 and 3.45 eV depending on the Ag content. It has been reported that heavy doping with Ag produces a blue shift of the NBE band, and, therefore, the band C can be associated with the Ag presence. The presence of band B suggests the existence of ZnO crystallites with different concentrations of Ag. An increase of the PL intensity was reported for Ag concentration up to 2.8%, while, for higher Ag concentrations, it decreases [39].The blue shift of the high-energy subband, C, increases from sample AZ1 to sample AZ4, furthermore, the PL intensity is concomitantly reduced, which is consistent with the scenario described in ref. [39] for the luminescence emission of Ag doped ZnO. In summary, the Ag incorporation in ZnO can induce a significant increase of the ZnO:Ag bandgap, and that up to 170 meV is observed for sample AZ4 with the highest Ag content. The blue-violet emission band A is associated with Zn interstitials [40]. The increase of the A band intensity with the concentration of Ag would suggest that the incorporation of Ag generates a significant concentration of Zn interstitials (Zn_i) as the blue-violet emission is associated with Zn_i [40,41]. The presence of Zn_i can also account for the low luminescence emission. In fact, the non-radiative recombination centers (NRRCs) were identified as Zn interstitial clusters[42–45].

Typical NBE PL spectra after annealing are shown in Fig. 7b. One can

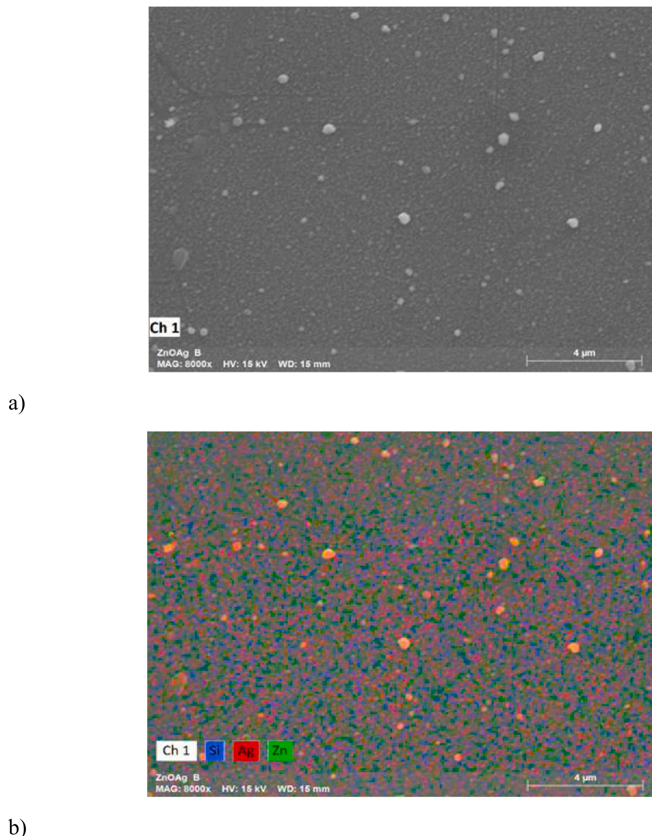

Fig. 6. a) SEM image from the surface of ZA1 film after annealing/reduction process. b) Superposition of imaging EDS analysis from the same sample with elemental composition map indicated by the label.

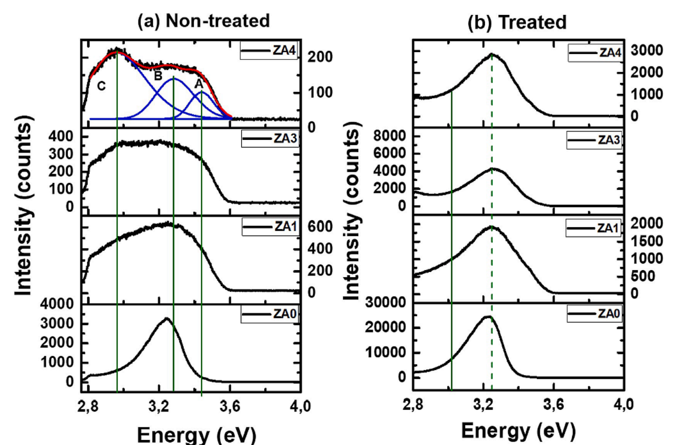

Fig. 7. a) PL spectra of ZA0 and ZA1, ZA3, and ZA4 before annealing treatment in the UV range. Vertical lines refer to the relevant peak positions from Gaussian fitting of ZA4 spectrum as reference. b) PL spectra of ZA0, ZA1, ZA3, and ZA4 after annealing in the UV range. The dashed vertical line is located around the estimated value of the pure ZnO sample (ZA0) band gap. All vertical lines are only guides to the eye.

observe a relevant increase of PL intensity for all the annealed samples with respect to the as-deposited samples. The ZnO sample exhibits a similar shape to the as-deposited one and only the intensity is increased. Furthermore, the spectra of the annealed samples of ZnO:Ag approach that of the reference ZnO sample and the NBE emission peaks are at 3.26 eV, while the high energy band, band C, associated to the presence of silver in the ZnO lattice is significantly reduced. This is a very relevant result because it evidences the segregation of silver under annealing, forming Ag crystals embedded in a ZnO matrix with some silver according to the residual band C observed in the annealed Ag-doped samples. See the high energy tail in the NBE spectra, in agreement with the previously described EDX results. The samples with a higher concentration of silver present lower NBE emission, which suggests a higher presence of non-radiative recombination centers, and a more disordered lattice for increasing Ag concentration. Furthermore, the blue-violet emission with band A, associated with Zni, is also quenched, suggesting that Zn ions recover its lattice site once the Ag atoms segregate. Zinc interstitials are fast diffusers unstable at room temperature [46], and, therefore, single Zni can be easily removed under annealing, and part of the Zni clusters seems to be disolved, which should account for the higher emission of the annealed samples.

In the visible range, the PL spectrum of ZnO before annealing consists of a broad yellow-orange (YL) band centered at 580 nm. The YL band was associated with either interstitial oxygen, Oi [40], or Li impurities [46] (see Fig. 8a). The Ag doped samples present a different spectrum with a very weak green emission (GL1), peaking at 510 nm (2.43 eV), and a red emission (RL) at 750 nm (1.65 eV). The origin of the GL is a matter of controversy, and different defects have been claimed to be responsible for this band [47]. One can distinguish two GL bands, one associated with copper impurities, Cu_{Zn}, and a second one associated with Oxygen vacancies, V_O [48,49]. The GL emission observed in the as-grown samples could be associated with residual copper impurities; we label it as GL1. There are two GL bands associated with Cu impurities: (i) an structured band with phonon replicas related to a localized excitation of a Cu^{2+} ion. An electron from a neighbor oxygen atom is transferred to the neutral Cu atom producing donor-hole recombination; and (ii) an unstructured band associated with a DAP transition involving Cu^{+} as the deep acceptor and a donor level [50]. The GL band observed in the as grown samples is not structured, which is the characteristic of the GL luminescence arising from the localized excitation of Cu^{2+} ions. However, when distorting the lattice by adding Ag, donors, e.g. Zni, can be formed and the DAP luminescence might account for the GL observed in the spectra of Fig. 8a.

The PL spectra in the visible range after annealing are shown in Fig. 8b. A great variation of the PL spectra with respect to the as-grown samples can be observed. The RL is quenched in the Ag-doped samples. The spectrum is dominated by green luminescence peaking at 526 nm (2.36 eV), which we label as GL2 in order to distinguish it from the copper related emission labeled GL1. GL2 is tentatively associated to V_O defects produced during the annealing in a reducing atmosphere, additionally, the annealing should reduce the donors responsible for the DAP transition. The quenching of the RL can be associated with the suppression of the V_{Zn}s by recombination with Zn_is.

The PL results evidence the segregation of Ag during the annealing as well as the diffusion of Zn_i, which replace the segregated Ag ions in the ZnO lattice, and also reduces the V_{Zn} quantity. The annealing used does not produce a full recovery of the ZnO lattice in Ag- doped samples, and, as it seems, the residual silver remain in ZnO after annealing.

The electrical transport properties of ZnO and ZnO:Ag thin films were analyzed by electrochemical impedance spectroscopy (EIS). The electrical parameters were obtained by fitting Nyquist plots to the suitable equivalent circuit model shown in Fig. 9a. As a result of the fitting process, the most suitable equivalent circuit model is composed of resistors (R), a capacitor (C) and a constant phase element (CPE) (Q). Accordingly, one circuit is Q//R in series with another R//C circuit, as presented in the inset of Fig. 9a. The first circuit (Q//R) corresponds to

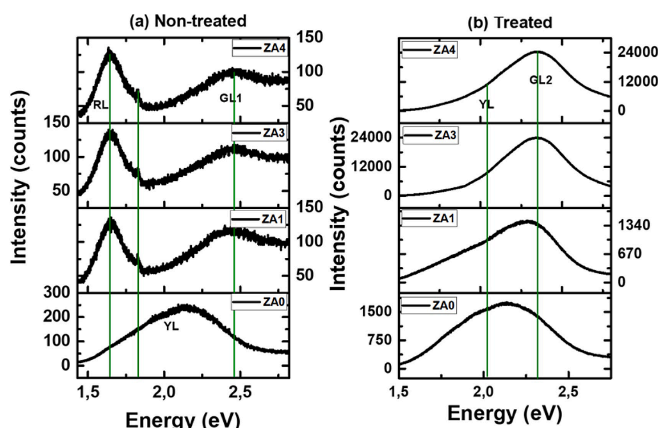

Fig. 8. a) PL spectra of ZA0, ZA1, ZA3 and ZA4 samples before annealing in the visible range. Continuous vertical lines refer to the relevant peak positions from Gaussian fitting of ZA4 spectrum before annealing taken as a reference. b) PL spectra of ZA0, ZA1, ZA3 and ZA4 samples after annealing in the visible range. All vertical lines are only guides to the eye.

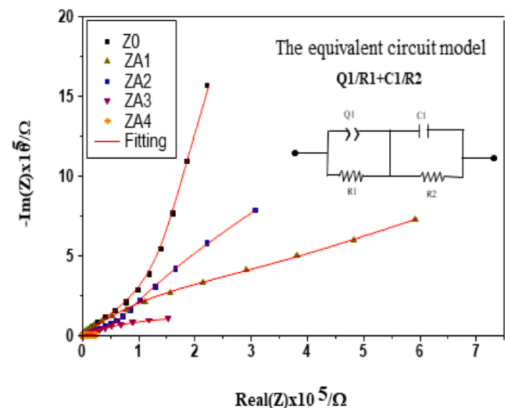

a)

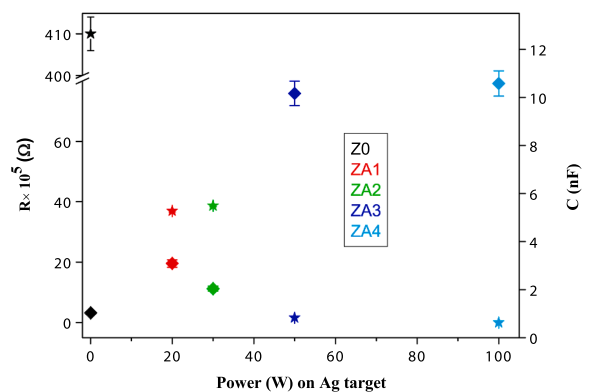

b)

Fig. 9. a) Nyquist plot corresponding to the samples. In the inset, the equivalent circuit model used for fitting curves is shown. b) RC elements for ZnO:Ag/Au interfaces. Resistor and Capacitor equivalent values as a function of the applied power on Ag target. The symbols ★ and ◆ represent the resistor and capacitor responses for each sample, respectively, identifying by the associated colors showed in the label inset.

the interface between silicon and ZnO:Ag thin films at low frequencies. While the second circuit (C//R) corresponds to the interface between ZnO:Ag and Au contact at high frequencies. Furthermore, the constant phase element in a circuit models an imperfect capacitor. Thus, its characteristic capacitor can be calculated from the following equation:

$$C = Q^{\frac{1}{a}} \bullet R^{\frac{1-a}{a}} \quad (2)$$

where Q is the CPE element and the factor α a is an index, which indicates the degree of “perfection” of this element. This index can vary between 0 and 1, with 0 describing a perfect resistor, and 1- a perfect capacitor [51].

A chart comparing the values of the resistance and capacitance as a function of the Ag target power for the ZnO:Ag/Au interface is displayed in Fig. 9b. It is clear that the values of the resistance decrease with increasing Ag target power. This behavior is attributed to the increase in the Ag metallic character of the ZnO:Ag composite, which was proven by RBS analysis and given in Fig. 2. Meanwhile, the capacitance increases for increasing Ag content. It is most important also to notice that the electrical conduction for the ZnO:Ag /Si interface improves with the increase in the power of Ag target during ZnO:Ag deposition. This behavior could be attributed to the in-depth gradient of Ag material through the thin films. The electrical parameters of the Si/ZnO:Ag and ZnO:Ag/Au interfaces for the fabricated samples are summarized in Table 2.

The electrical behavior of thin films after annealing in a hydrogen atmosphere was determined using the two-point probe method. The current-Voltage (I-V) measurements provide a linear relation shown in Fig. 10, leading to an ohmic electrical behavior, except for the pure ZnO thin film, which shows a Schottky behavior as given in the inset. Accordingly, the experimental data for the composite samples were fitted to a linear regression, from which the values of the electrical conductivity were extracted using the Ohm law.

As a comparison between the electrical resistance before treatment and after, the experimental results show that the thermal processing has a notable effect on the conductivity of the ZnO and ZnO:Ag composite thin films. The large enhancement is attributed to the aggregation of metallic Ag in the films. Furthermore, the increase in the power of the Silver target leads to an increase in the conductivity of the thin film, as given in Fig. 10a. Complementarily, the electrical improvement could be attributed to the oxygen deficiency reached during treatment in H_2 atmosphere. As a result, metallic Ag and clusters and ZnO_x:Ag, $x < 1$, might represent the majority of the thin film composite.

4. Summary and conclusions

In this work different material characterization techniques, namely, XRD, RBS, Ellipsometry, Photoluminescence and electrical measurements has been obtained to study the properties of ZnO:Ag thin films grown by DC magnetron sputtering with the use of independent Zn and Ag targets in oxygen/argon atmosphere. Presently, there exist a scarce information on using this growth technique for this kind of samples. However, it allows much better control on the deposited species. The applied power on Zn target was kept at 100 W, while the power applied on Ag target was varied from 20 to 100 W. Thus, the thicknesses of the samples were below 200 nm, as measured with profilometry and it is in well agreement with the ones estimated from RBS results. It was verified that the higher the power applied on Silver target, the higher Silver content in the films getting significant changes in the physical properties of the as grown samples. In fact, the Ag incorporation in the ZnO films produces the amorphization of ZnO. The incipient amorphous phases of silver seem to appear at the highest silver content.

Thermal treatments of the samples in a reducing atmosphere at 300 °C promotes a clear recrystallization of the samples favoring the growth of cubic Ag phase hosted by the ZnO hexagonal wurtzite phase, as shown by XRD measurements. The PL spectra are coherent with a decrease of the amount of Ag atoms embedded in the ZnO crystalline structure and they evidence a significant reduction of the C labeled band associated with the presence of Ag in the ZnO matrix; this complements the XRD results, as it confirms the Ag segregation in the annealed samples. Besides, the blue band is also quenched indicating that Zn ions recover their lattice sites once the substitutional Ag atoms have been segregated. The presence of a weak contribution of the PL band associated to the presence of silver in the ZnO lattice in the annealed samples permits to assume that the thermal treatment does not allow the full segregation of Ag, and there are vestiges of silver in the ZnO lattice. The PL spectra recorded after annealing also indicate a significant reduction of defects. A Silver plasmonic effect has been identified in all of the annealed samples from the features of ellipsometric functions around 300 nm. Electrical measurements confirm the great variation produced by the annealing treatment in the electrical conductivity of the samples,

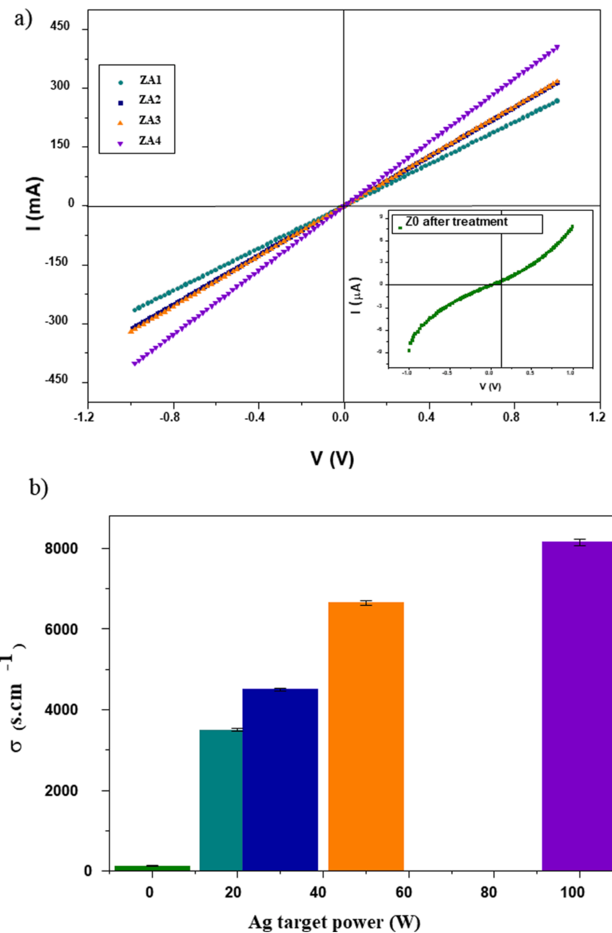

Fig. 10. a) I–V curves for ZnO: Ag samples annealed in H_2 atmosphere as compared to pure ZnO sample (inset). b) Map for the electrical conductivity of the annealed thin films as a function of the applied Ag power during deposition process.

Table 2
Comparison between the equivalent circuit elements for the pure ZnO and ZnO: Ag samples.

Sample	R1×10^5 (Ω)	Q1 (nF.S^{a-1})	a1	C1 (uF)	R2×10^5 (Ω)	C2 (nF)
Si/ZnO:Ag interface					ZnO:Ag/Au interface	
Z0	1.87	9.91	0.75	1.2	410	1.03
ZA1	7.32	4.60	0.78	3.8	36.95	3.09
ZA2	2.24	45.10	0.59	8.37	38.70	2.04
ZA3	0.89	37.5	0.70	2.34	1.64	10.17
ZA4	0.23	0.15	0.65	5.93	0.03	10.58

which varies by an order of magnitude. The results presented in this work suggest that DC Magnetron Sputtering ZnO:Ag samples with optimal plasmonic behavior can be achieved by controlling the Ag concentration, and the annealing conditions.

Declaration of Competing Interest

The authors declare that they have no known competing financial interests or personal relationships that could have appeared to influence the work reported in this paper.

Acknowledgments

This work was supported by the Ministerio de Ciencia, Innovación y Universidades of Spain through the Project RTI2018-095137-B-I00 with partial contributions from project IND2019/IND-17155 specifically, around the Optoelectronic applications of these materials. SD and JJ were funded by Junta de Castilla y León (Project VA283P18)

References

[1] Di Mauro, M. Cantarella, G. Nicotra, V. Privitera, G.Impellizzeri, Appl. Catal. B: Environm. 196 (2016) 68. https://doi.org/10.1016/j.apcatb.2016.05.015.
[2] Y. Xia, J. Wang, R. Chen, D. Zhou, L. Xiang, Crystals 6 (2016) 148, https://doi.org/10.3390/cryst6110148.
[3] V. Shukla, A. Patel, Nanosyst. Phys. Chem. Math. 11(2020), 391. https://doi.org/10.17586/2220-8054-2020-11-4-391-400.
[4] M. Yuste, R. Escobar Galindo, I. Caretti, R. Torres, O. Sanchez, J. Phys. D: Appl. Phys. 45 (2012), 025303, https://doi.org/10.1088/0022-3727/45/2/025303.
[5] R. Ramadan, D. Romera, R. Delgado Carrascon, M. Cantero, J.-J. Aguilera-Correa, J.P. García Ruiz, J. Esteban, M. Manso Silvań, ACS Omega 4 (2019) 11354, https://doi.org/10.1021/acsomega.9b00646.
[6] R. Perumal, S. Thanikaikarasan, R. Saravannan, V. Vijayan, Materials Today: Proceedings 21 (2020) 912.
[7] T. Abu Ali, JuliaT. Abu Ali, J. Pilz ,P. Schäffner, M. Kratzer, C. Teichert, B. Stadlober, and A.M. Coclite, Phys. Status Solidi A 217,(2020), 2000319 https://doi.org/10.1002/pssa.202000319.
[8] G.K. Weldegebrieal, Inorgan. Chem. Commun. 120 (2020), 108140, https://doi.org/10.1016/j.inoche.2020.108140.
[9] I.V. Nain, M. Kaur, K.S. Sandhu, R. Thory, A. Sinhmar, Int. J. Biol. Macromol. 162 (2020) 24, https://doi.org/10.1016/j.ijbiomac.2020.06.125.
[10] Q. Tang, X. Chen, J.X. Wan, H. Wu, C.Liu. IEEE Trans. Electron Devices (2020) 3129. 1https://doi.org/0.1109/JEDS.2020.3034387.
[11] C.Li, XH. Fan,LM. Yu,L. Cui, ML.Yin,Y. Li, N.Nan,N. Liu, Opt. Mater. 103 (2020) 109891, https://doi.org/10.1016/j.optmat.2020.109891.
[12] YW. Pan, SJ .Peng,YL. Ma, P J. Cao, F. Hu. J. Nanosci. Nanotechnol. 20, (2020), 7800, https://doi.org/10.1166/jnn.2020.18890.
[13] D. Chen, Y. Xin, B. Lu, X. Pan, J. Huang, H. He, Z. Ye, Appl. Surf. Sci. 529 (2020), 147087, https://doi.org/10.1016/j.apsusc.2020.147087.
[14] M. Shkira, B.M. Al-Shehri, M.P. Pachamuthu, A. Khan, K.V. Chandekar, S. AlFaify, M.S. Hamdy, Colloids Surf. A Physicochem. Eng. Aspects 587 (2020), 124340, https://doi.org/10.1016/j.colsurfa.2019.124340.
[15] Zheng Yang. Appl Phys A, 112 (2013) 241. 1https://doi.org/0.1007/s00339-013-7658-7.
[16] A. Karami, Z. Xie, J. Zhang, M.S. Kabir, P. Munroe, S. Kidd, H. Zhanga, Mater. Sci. Eng. C 107 (2020), 110220, https://doi.org/10.1016/j.msec.2019.110220.
[17] J. Panigrahi, D. Behera, I. Mohanty, U. Subudhi, B.B. Nayak, B.S. Acharya, Appl. Surf. Sci. 258 (2011) 304, https://doi.org/10.1016/j.apsusc.2011.08.056.
[18] M. Mirhosseini, F.B. Firouzabadi, Int. J. Dairy Technol. 66 (2013) 291, https://doi.org/10.1111/1471-0307.12015.
[19] L.Chen, X. Zhang, Z. Xiong, Y. Liu, Y. Cui, B. Liu J. Alloys Compounds,798 (2019) 149, https://doi.org/10.1016/j.jallcom.2019.05.257.
[20] F.Hashim, A. F. Alkaim, S. J. Salim, A.l H. Omran Alkhayatt. Chem. Phys. Lett. 737 (2019)136828, https://doi.org/10.1016/j.cplett.2019.136828.
[21] S. Choudhary, V. Kumar, V. Malik, R. Nagarajan, S. Annapoorni, R. Malik, J. Phys.: Condens. Matter 32 (2020), 405202, https://doi.org/10.1088/1361-648X/ab9e2e.
[22] S. Koppala, Y. Xia, L. Zhang, J. Peng, Z. Chen, L. Xu, Ceram. Int. 45 (2019) 15116, https://doi.org/10.1016/j.ceramint.2019.04.252.
[23] H. Liu, Y. Hu, Z. Zhang, X. Liu, H. Jia, B. Xu, Appl. Surf. Sci. 355 (2015) 644, https://doi.org/10.1016/j.apsusc.2015.07.012.
[24] J.C. Jaramillo-Páeza, J.A. Navío, M.C. Hidalgo, J. Photochem. Photobiol. A Chem. 356 (2018) 112, https://doi.org/10.1016/j.jphotochem.2017.12.044.
[25] K.-T. Chuang, H. Abdullah, S.-J. Leu, K.-B. Cheng, D.-H. Kuo, H.-C. Chen, J.-H. Chien, W.-T. Hu, J. Photochem. Photobiol. A Chem. 337 (2017) 151–164, https://doi.org/10.1016/j.jphotochem.2017.01.012.
[26] S.K. Singh, R. Singhal, Thin Solid Films 653 (2018) 377, https://doi.org/10.1016/j.tsf.2018.03.063.
[27] H.S. Kang, B.D. Ahn, J.H. Kim, G.H. Kim, S.H. Lim, H.W. Chang, S.Y. Lee, Applied Physics Letters 88 (2006), 202108, https://doi.org/10.1063/1.2203952.
[28] H. Lu, X .Li, Z. Zhang, G. Shao Materials research innovations, 23 (2019) 129 https://doi.org/10.1080/14328917.2017.1395979.
[29] Y.-C. Chang, Sensors and Actuators B 225 (2016) 498, https://doi.org/10.1016/j.snb.2015.11.053.
[30] F.-C. Liu, J-Y Li 1, T-H Chen, C-H Chang, C-T Lee, W-H Hsiao, D-S Liu. Materials 10 (2017) 797, https://doi.org/10.3390/ma10070797.
[31] M. Mayer, SIMNRA User's Guide 7.02, Max-Planck-Institut für Plasmaphysik, Garching, Germany, 2019.
[32] R.E. Treharne, A. Seymour-Pierce, K. Durose, K. Hutchings, S. Roncallo, D. Lane, J. Phys, Conf. Ser. 286 (2011), 012038.
[33] PCPDFWIN version 2.2 © 2001 JCPDS-ICDD http://www.icdd.com.
[34] D. Toledano, R. Escobar Galindo, M. Yuste, J.M. Albella, O. Sánchez, J. Phys. D: Appl. Phys. 46 (2013), 045306, https://doi.org/10.1088/0022-3727/46/4/045306.
[35] L. Xua, F. Xian, Y. Zhang, L. Zhang, Physica B: Condensed Matter 566 (2019) 103, https://doi.org/10.1016/j.physb.2019.05.007.
[36] L.V. Azaroff, Elements of X- Ray Cryctallography, McGraw-Hill Inc, 1968.
[37] O. Aguilar, S. de Castro, M.P.F. Godoy, M.R.S. Dias, Opt. Mater. Express 9 (2019) 3638, https://doi.org/10.1364/OME.9.003638.
[38] W. Shan, W. Walukiewicz, J.W. Ager III, K.M. YuH, B. Yuan, H.P. Xin, G. CantwellJ, J. Song. Appl. Phys. Lett. 86 (2005), 191911, https://doi.org/10.1063/1.1923757.
[39] X.B. Wang, C. Song, K.W. Geng, F. Zeng, F. Pan, J. Phys. D: Appl. Phys. 39 (2006) 4992, https://doi.org/10.1088/0022-3727/39/23/014.
[40] H. Zeng, G. duan, Y. Li, S. Yang, X. Xu, W. Cai. Adv. Funct. Mater. 20 (2010) 561 https://doi.org/10.1002/adfm.200901884.
[41] L.E. Halliburton, N.C. Giles, N.Y. Garces, M. Luo, C. Xu, L. Bai, L.A. Boatne, Appl. Phys. Lett. 87 (2005), 172108, https://doi.org/10.1063/1.2117630.
[42] D.N. Montenegro, V. Hortelano, O. Martínez, M.C. Martínez-Tomas, V. Sallet, V. Muñoz-Sanjosé, J. Jiménez, J. Appl. Phys. 113 (2013), 143513, https://doi.org/10.1063/1.4801534.
[43] D.N. Montenegro, V. Hortelano, O. Martínez, M.C. Martínez-Tomas, V. Sallet, V. Muñoz-Sanjosé, J. Jiménez, J. Phys. D: Appl. Phys. 46 (2013), 235302, https://doi.org/10.1088/0022-3727/46/23/235302.
[44] M.A. Gluba, N.H. Nickel, N. Karpensky. Phys.Rev.B 88 (2013)245201. 1https://doi.org/0.1103/PhysRevB.88.245201.
[45] M.D. McCluskey, S.J. Jokela; Appl. Phys. Rev. 106 (2009) 071101). https://doi.org/10.1063/1.3216464.
[46] U. Ozgur, Y.Alivov, C.Liu, A. Teke, M. Reshchikov, S. Dogan, V. Avrutin, S. Cho, H. Morkoc; J. Appl. Phys. 98 (2005) 041301. 1https://doi.org/0.1063/1.1992666.
[47] M.A. Reshchikov, H. Morkoc, B. Nemeth, J. Nause, J. Xie, B. Hertog, A. Osinsky, Physica B 401–402 (2007) 358, https://doi.org/10.1016/j.physb.2007.08.187.
[48] J. Mass, M. Avella, J. Jimenez, M. Callahan, E. Grant, K. Rakes, D. Bliss, B. Wang; New materials and Processes for incoming semiconductor technologies; Ed. by S. Dueñas. Transworld Research Network (Kerala 2006) p113.
[49] K. Vanheusden, W.L. Warren, C.H. Seager, D.R. Tallant, J.A. Voigt, B.E. Genade, J. Appl. Phys. 79 (1996) 7983.
[50] N.Y.Garces, L.Wang, L.Bai, N.C. Giles, L. E. Halliburton, and G. Cantwell., Appl. Phys. Lett. 81, 622 (2002).
[51] M.E. Orazem, B. Tribollet, Electrochemical Impedance Spectroscopy; JohnWiley & Sons: Hoboken, NJ, USA, 2017.